Quantum anomalous Hall octet driven by orbital magnetism in bilayer graphene

https://doi.org/10.1038/s41586-021-03849-w

Received: 16 April 2021

Accepted: 22 July 2021

Published online: 6 October 2021

Check for updates

Fabian R. Geisenhof[1], Felix Winterer[1], Anna M. Seiler[1], Jakob Lenz[1], Tianyi Xu[2], Fan Zhang[2]✉ & R. Thomas Weitz[1,3,4,5]✉

The quantum anomalous Hall (QAH) effect—a macroscopic manifestation of chiral band topology at zero magnetic field—has been experimentally realized only by the magnetic doping of topological insulators[1–3] and the delicate design of moiré heterostructures[4–8]. However, the seemingly simple bilayer graphene without magnetic doping or moiré engineering has long been predicted to host competing ordered states with QAH effects[9–11]. Here we explore states in bilayer graphene with a conductance of $2\,e^2\,h^{-1}$ (where e is the electronic charge and h is Planck's constant) that not only survive down to anomalously small magnetic fields and up to temperatures of five kelvin but also exhibit magnetic hysteresis. Together, the experimental signatures provide compelling evidence for orbital-magnetism-driven QAH behaviour that is tunable via electric and magnetic fields as well as carrier sign. The observed octet of QAH phases is distinct from previous observations owing to its peculiar ferrimagnetic and ferrielectric order that is characterized by quantized anomalous charge, spin, valley and spin–valley Hall behaviour[9].

Intricate interplay between single-particle effects such as the band topology and many-body effects such as the electron–electron interaction determines the electronic ground states of many low-dimensional systems. An especially interesting class are systems in which quasiparticle Berry curvature gives rise to orbital instead of spin magnetic moments, with the consequence that effects usually requiring substantial spin–orbit coupling and/or intentional magnetic doping can occur spontaneously[9,10]. A prominent example is the quantum anomalous Hall (QAH) phase that displays quantized Hall resistance at zero magnetic field owing to the presence of orbital magnetic order. The QAH effect is characterized by a finite number of topologically protected chiral edge channels. So far, it has been experimentally realized in two distinct types of systems. In magnetically doped topological insulators[1–3], topological properties and broken time-reversal symmetry (caused by spin–orbit coupling and aligned magnetic dopants, respectively) lead to topologically non-trivial Chern bands[12,13]. In these spin Chern insulators, magnetism occurs mainly owing to ordering of electron spin moments. However, a Chern insulator can also emerge solely owing to a spontaneous polarization of the orbital magnetic moments[9,10,14], as recently observed in delicately designed moiré heterostructures[4–8]. In these orbital Chern insulators, orbital magnetism arises because of spontaneous gap opening in the half-filled quasiparticle Dirac bands[9–11,14]. Gapped Dirac bands with non-trivial Berry-curvature-induced orbital magnetic moments have also been predicted[9,15] and observed in naturally occurring purely carbon-based systems such as bilayer graphene[16,17] and its rhombohedral cousins[18]. However, orbital magnetism[9] has not been clearly pinpointed experimentally in such a simple system as pure bilayer graphene, despite theoretical studies[9–11] predicting that some of the competing ground states should exhibit non-vanishing exchange-interaction-driven quantized Hall conductivities at zero magnetic field.

Here we report the observation of filling factor $\nu = \pm 2$ states at anomalously small magnetic fields of about 20 mT in suspended dually gated bilayer graphene devices. In addition, we observe field tuning and magnetic hysteresis, which strongly evidences that the $\nu = \pm 2$ states are ferrimagnetic, ferrielectric, QAH phases driven by orbital magnetism in pure bilayer graphene. Using bilayer graphene flakes free of electronically active domain walls[19–21] and previously established processing[22] (Methods, Extended Data Fig. 1), suspended dually gated bilayer graphene devices were fabricated (Fig. 1a).

Sweeping both top and bottom gate voltages, V_t and V_b, at zero magnetic field yields the well known map of the differential conductance, including the interlayer electric-field-induced insulating states as well as the exchange-interaction-induced gapped phase near zero electric field (Fig. 1b)[23–25]. The observation of the latter and the location of the charge neutrality point at $V_t \approx V_b \approx 0$ demonstrates the high quality of the device (note that such a spontaneous gap is universal for rhombohedral few-layer and Bernal even-layer graphene[9,18,26]). The dual-gate structure allows independent tunability of the charge carrier density n and the perpendicular electric field $E_\perp$ (Methods). Sweeping n at $E_\perp = 0$ reveals a residual charge density inhomogeneity of less than 10^9 cm^{-2} (Fig. 1b, inset), underlining the high quality of the device[27] (Methods).

Varying both n and $E_\perp$ while applying a perpendicular magnetic field of $B = 3$ T (Fig. 1c) reveals the lowest quantum Hall plateaus in bilayer graphene with the integer filling factors ranging from $\nu = -4$ to $\nu = 4$ (refs. [23,28–32]), resulting from the spontaneous symmetry breaking in the anomalous $N = 0$ Landau levels. As identified previously, only the $\nu = 0$ and $\nu = \pm 4$ quantum Hall states are resolved at $E_\perp = 0$ (Fig. 1c), whereas

[1]Physics of Nanosystems, Department of Physics, Ludwig-Maximilians-Universität München, Munich, Germany. [2]Department of Physics, University of Texas at Dallas, Richardson, TX, USA. [3]Center for Nanoscience (CeNS), Munich, Germany. [4]Munich Center for Quantum Science and Technology (MCQST), Munich, Germany. [5]1st Physical Institute, Faculty of Physics, University of Göttingen, Göttingen, Germany. ✉e-mail: zhang@utdallas.edu; thomas.weitz@uni-goettingen.de

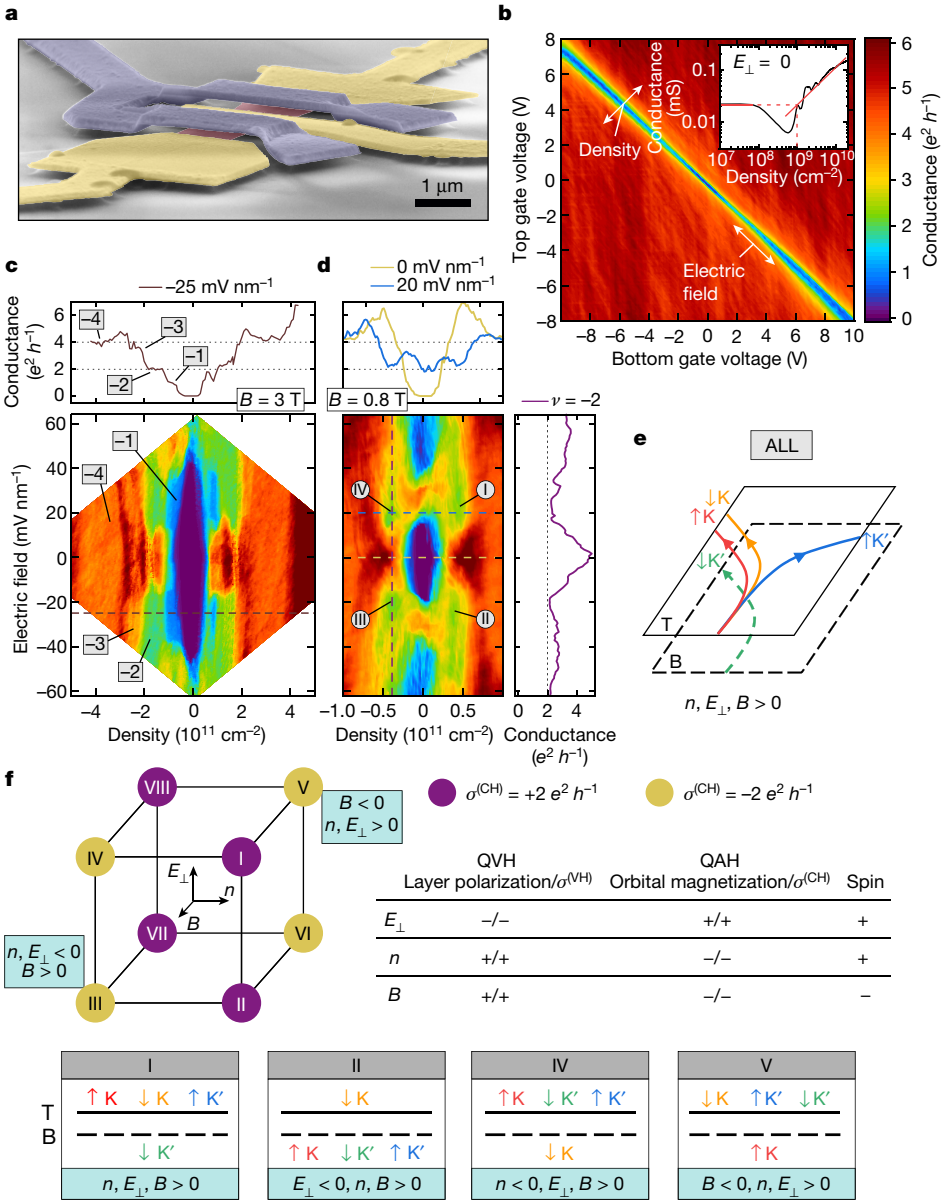

Fig. 1 | Exchange-interaction-driven quantum Hall states in dually gated, freestanding bilayer graphene. a, False-colour scanning electron microscope image of a suspended bilayer graphene device. Contacts, top gate and bilayer graphene are shown in yellow, blue and red, respectively. **b**, Conductance map as a function of top gate voltage and bottom gate voltage at $B = 0$ and $T < 10$ mK. Inset: conductance as a function of charge carrier density at $E_\perp = 0$. The red lines are linear fits and the dashed red lines are guides to the eye, indicating the residual charge carrier inhomogeneity in the device. **c**, **d**, Maps of the conductance as a function of $E_\perp$ and n at $B = 3$ T (**c**) and $B = 0.8$ T (**d**). The roman numerals in **d** label the 'ALL' phases labelled by the same numerals in **f**. **e**, Schematic representation of one 'ALL' QAH phase showing the classical counterpart of its corresponding spontaneous quantum Hall effect for $n, E_\perp, B > 0$. T and B refer to the top and bottom graphene layers, respectively. **f**, Top: schematic of the eight different 'ALL' phases and their corresponding Hall conductance $\sigma^{(CH)}$ and how they can be accessed by tuning $n, E_\perp$ and/or B. The table shows the properties of the QVH and QAH species of the 'ALL' octet: the layer polarization and orbital magnetization as well as the valley and charge Hall conductivities, $\sigma^{(VH)}$ and $\sigma^{(CH)}$. +/− indicates whether the observables are even/odd under flipping $n, E_\perp$ or B. Bottom: schematics of the layer polarizations of the four spin–valley species for four exemplary 'ALL' phases.

the $\nu = \pm1$, $\nu = \pm2$ and $\nu = \pm3$ states emerge only at a larger finite electric field[23,32,33]. At a lower magnetic field of $B = 0.8$ T (Fig. 1d), only the $\nu = 0$, $\nu = \pm2$ and $\nu = \pm4$ states emerge. Surprisingly, in contrast to the $\nu = \pm4$ states, the $\nu = \pm2$ states are only stable in an intermediate range of electric field (four green regions in Fig. 1d), that is, both larger and smaller electric fields can destabilize the $\nu = \pm2$ states.

QAH phases in bilayer graphene

Although the $\nu = \pm2$ states in bilayer graphene have been observed previously at $B > 1.2$ T (refs. [23,32]), their exact nature—especially with lowering the magnetic field towards the $B = 0$ limit where one can expect intricate QAH phases and phase transitions as function of electric field—has not been identified previously. The order parameters of these states are particularly interesting, as they can unveil the yet unclear ground state of bilayer graphene in the $B = 0$ limit[9–11,34]. Owing to the quadratic band touching and non-trivial winding numbers, the exchange interaction in bilayer graphene is peculiarly strong and produces non-trivial quasiparticle topological properties[10]; various symmetry-broken states have been suggested as gapped competing ground states[9,11] (Methods, Extended Data Fig. 2, Table 1), with two families of QAH phases exhibiting orbital magnetism[9]. One family manifesting a Hall conductance of 4 e^2 h^{-1} (where

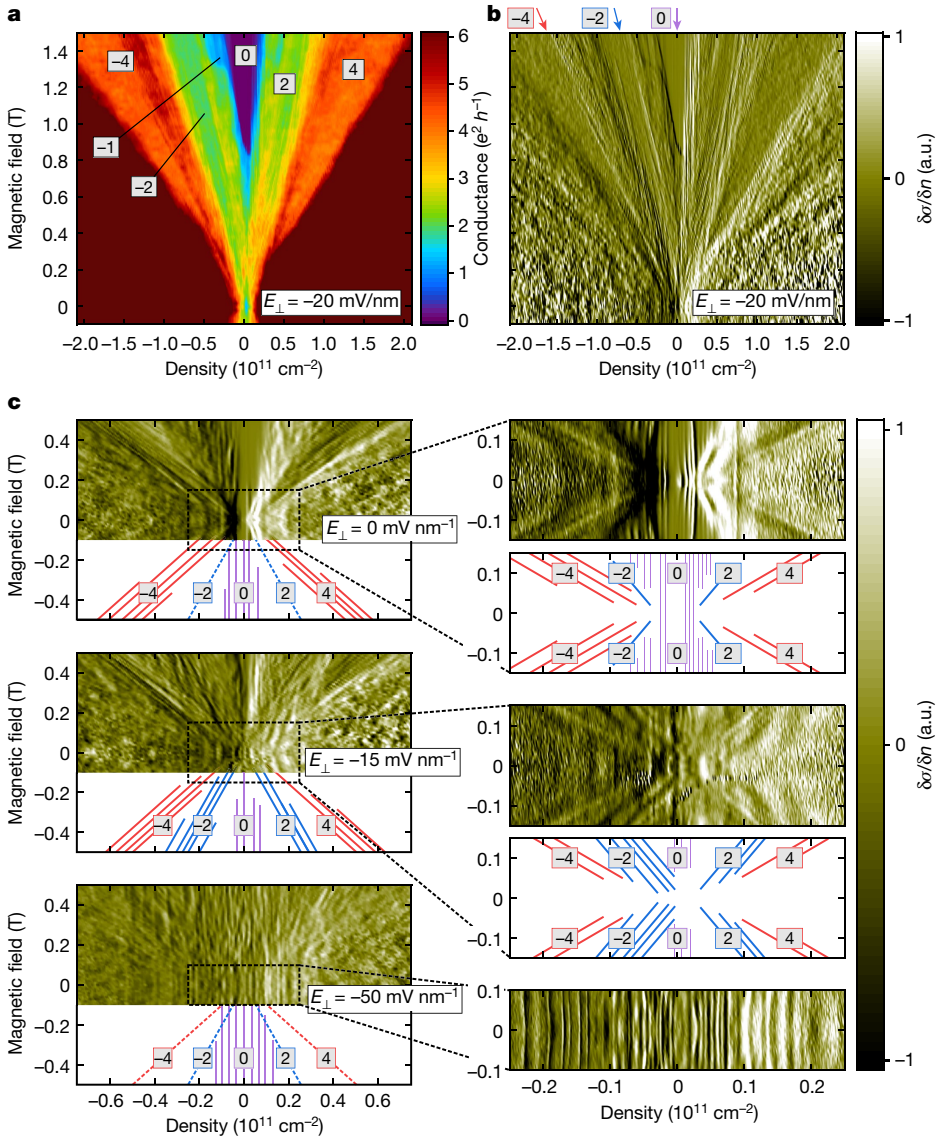

Fig. 2 | Extraordinary stability of the tunable $\nu = \pm 2$ quantum Hall states towards zero magnetic field. a, **b**, Fan diagrams of the differential conductance (**a**) and its derivative $\delta\sigma/\delta n$ (**b**) at $E_\perp = -20$ mV nm^{-1}. The slopes of the $\nu = 0$, $\nu = -2$ and $\nu = -4$ states are indicated with purple, blue and red arrows, respectively. **c**, Left: $\delta\sigma/\delta n$ plotted as a function of magnetic field and density for various $E_\perp$. Right: high-resolution measurements around zero magnetic field. The schematics indicate transconductance fluctuations corresponding to the $\nu = 0$, $\nu = -2$ and $\nu = -4$ states that are shown with purple, blue and red lines, respectively. Solid (dashed) lines indicate the slopes of the respective states in case they are present (absent). All measurements were taken at $T < 10$ mK.

e is the electronic charge and h is Planck's constant), simply termed the QAH phase, is a bilayer counterpart of the Haldane QAH state, in which electrons from different valleys spontaneously polarize to different layers resulting in a Z_2 orbital ferromagnetic order. The other family manifesting Hall conductance of $2\,e^2\,h^{-1}$, termed the 'ALL' phase[9], is even more exotic; as quasiparticles of one spin can choose either one of the two quantum valley Hall (QVH) phases—electrons from both valleys polarize to the same layer resulting in a Z_2 ferroelectric order—whereas quasiparticles of the other spin can choose either one of the two aforementioned QAH phases (Fig. 1e, Methods, Extended Data Fig. 2). In total, there are eight different ALL phases forming an octet with Chern number $C = \pm 2$ or Hall conductance $\sigma^{(CH)} = \pm 2\,e^2\,h^{-1}$ (Extended Data Fig. 3). Markedly, each ALL phase exhibits quantized anomalous charge, spin, valley and spin–valley Hall effects and hence the name[9,10]. Owing to its partial layer polarization, each ALL phase can be stabilized with an interlayer electric field, which fits well with our observations. At very high electric fields, the phase vanishes again, losing stability against a fully layer-polarized QVH phase. Furthermore, applying a perpendicular magnetic field should lower its energy as the field can couple to the quasiparticle orbital magnetization[9,10]. Therefore, switching the sign(s) of the applied n, $E_\perp$ and/or B results in a quantum phase transition between two different ALL phases, as sketched in Fig. 1f. By flipping $E_\perp$ and n, the layer polarization of the QVH species and the orbital magnetization of the QAH species become opposite, respectively. By flipping B, both the orbital magnetization and the spin of the QAH species become opposite. Comparing the measurement at $B = 3$ T (Fig. 1c) and $B = 0.8$ T (Fig. 1d), we find that the electric field range at which the octet emerges at $B = 3$ T expands towards higher electric fields. This demonstrates the enhanced stability of the octet with increasing magnetic field (see Extended Data Fig. 4 for more data on the evolution of these phases in magnetic field).

Tracing the $\nu = \pm 2$ QAH phases to $B = 0$

So far, we have examined the stability of the $\nu = \pm 2$ QAH phases at small but finite magnetic fields. As these phases are driven by the exchange-interaction-induced orbital magnetism, they should, however, also

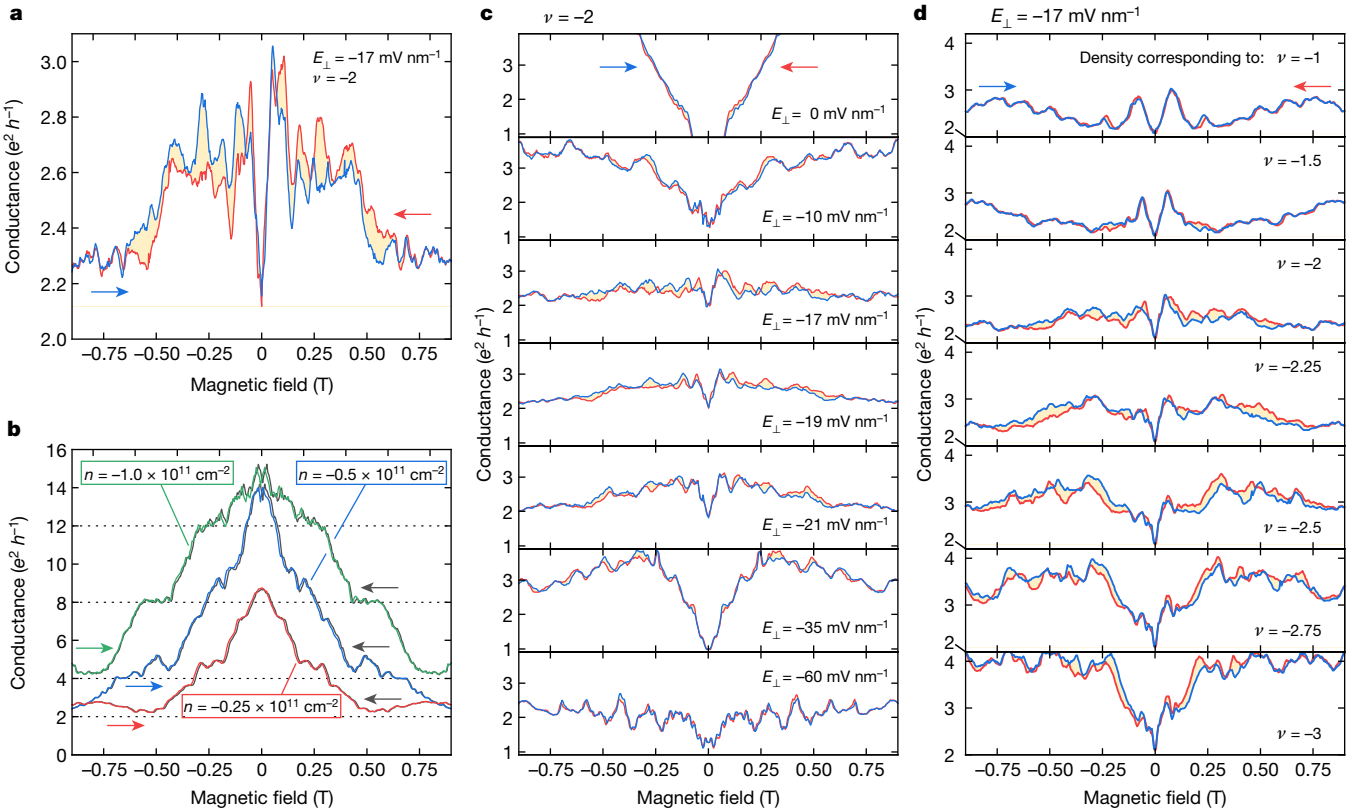

Fig. 3 | Magnetic hysteresis observable in the quantum anomalous Hall ν = −2 in bilayer graphene. a, Two-terminal conductance hysteresis measured for ν = −2 and $E_\perp$ = −17 mV nm^{-1}. The hysteresis loop area is shaded for clarity. The blue and red arrows indicate the forward and reverse sweep, respectively. **b**, Magnetic field dependence of the conductance measured for variable filling factor but fixed charge carrier density at $E_\perp$ = −17 mV nm^{-1}. The forward sweep for $n = -0.25 \times 10^{11}$ cm^{-2}, $n = -0.5 \times 10^{11}$ cm^{-2} and $n = -1.0 \times 10^{11}$ cm^{-2} is shown in red, blue and green, respectively. The reverse sweeps are shown in black. **c**, **d**, Hysteresis of the conductance as a function of electric field at fixed ν = −2 (**c**) and for various filling factors at fixed $E_\perp$ = −17 mV nm^{-1} (**d**). Note that the varying ν in **d** labels the ν = −2 phase at slightly different densities rather than different quantum Hall states. The forward and reverse sweeps are shown in blue and red, respectively, as indicated by the arrows. All measurements were taken at $T < 10$ mK.

be stable towards $B = 0$. To this end, we have recorded multiple fan diagrams around $B = 0$ at various electric fields (Fig. 2). From the fan diagram at $E_\perp = -20$ mV nm^{-1} (Fig. 2a, b) we can see that both the $\nu = \pm 2$ and $\nu = \pm 4$ states emerge already at unusually small magnetic field. We focus here on the $\nu = \pm 2$ QAH phases, as they previously escaped observation at such low magnetic fields[30,32,35], and because they are the most exotic ones among the competing ground states of bilayer graphene at $B = 0$: quasiparticles of one spin form a QVH phase whereas those of the other spin form a QAH phase[9–11] (Fig. 1e, Methods). Carefully examining the derivative of the conductance (Fig. 2b) to track fluctuations near incompressible quantum states provides more insight[36,37], as the traceable fluctuations are assignable to specific filling factors using their slopes and can appear even before the corresponding quantum Hall states emerge in conventional magneto-transport measurements. Investigating the derivative of the differential conductance at various electric fields (Fig. 2b, c) demonstrates that both the $\nu = \pm 2$ and $\nu = \pm 4$ states already emerge at magnetic fields well below $B = 100$ mT, but that they differ in their electric field dependences. In contrast to the number of fluctuations at finite B corresponding to the $\nu = \pm 4$ states, which decreases with increasing negative electric field (Fig. 2c, left), the $\nu = \pm 2$ states are prominent at $E_\perp = -15$ mV nm^{-1} but disappear at zero and very high negative electric fields. In addition, high-resolution scans around zero magnetic field (Fig. 2c, right) reveal that the $\nu = \pm 2$ states are also present for $B < 100$ mT. In fact, they do persist to $B < 20$ mT, which is even further than the $\nu = \pm 4$ states. This provides strong evidence that the QAH $\nu = \pm 2$ phases are potential ground states of bilayer graphene at $B = 0$ in addition to the previously identified $\nu = 0$ layer antiferromagnet (LAF) and $\nu = \pm 4$ QAH phases[23–25,30,35].

The observation that the $\nu = \pm 2$ states can be stabilized by a combination of B and $E_\perp$ fields is consistent with their partial layer polarizations and orbital magnetic characters. Finally, for very high electric fields, fluctuations with an infinite slope that trace the fully layer-polarized $\nu = 0$ QVH phase dominate the fan diagram (see Extended Data Fig. 5 for more data showing fan diagrams in electric fields).

Orbital-magnetism-driven hysteresis

Although the electric and magnetic field dependences and the stability down to $B \approx 0$ T support the presence of the QAH phases, we have looked for more direct proof of the presence of their orbital magnetism. Indeed, hysteretic behaviour indicative of magnetism is observable in the samples, even though in our two-terminal measurements the absolute contributions of both longitudinal and Hall resistances are measured simultaneously (Methods). As can be seen in Fig 3a, by sweeping the magnetic field at constant $\nu = -2$ and $E_\perp = -17$ mV nm^{-1}, we have recorded a magnetic hysteresis. Forward and reverse sweeps are mirror symmetric with respect to the $B = 0$ line, with the hysteretic behaviour starting at about $B = \pm 650$ mT. In addition, the hysteresis is highly reproducible upon repeated sweeps and we also observe it in a second device (Extended Data Fig. 6). Sweeping a smaller range than that between $B = \pm 650$ mT reduces the hysteresis (Extended Data Fig. 7). This magnetic hysteresis provides consistent evidence for the emergence of orbital magnetism in pure bilayer graphene; notably, such hysteretic behaviour is rare for moiréless purely carbon-based two-dimensional systems[18]. Given the vanishing spin–orbit coupling in bilayer graphene, the magnetism is primarily of orbital nature, which

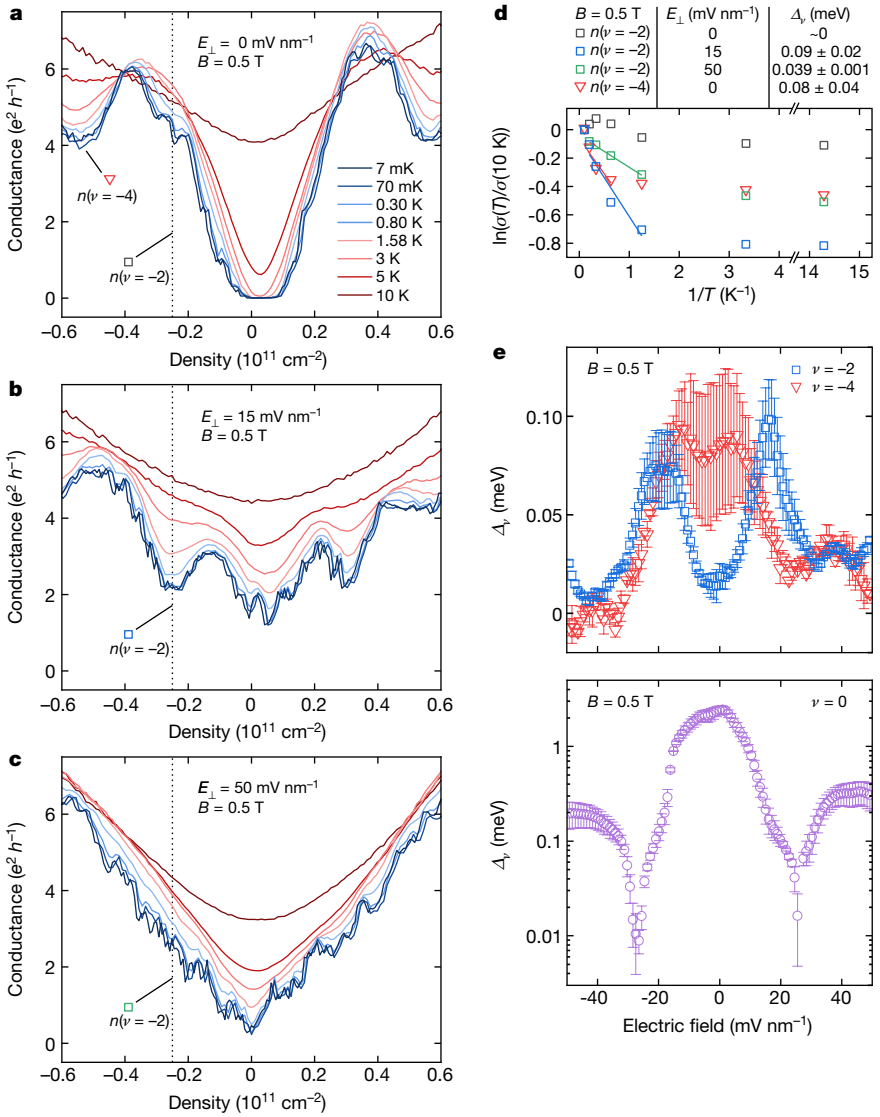

Fig. 4 | Temperature dependence of the $\nu = \pm 2$ and $\nu = \pm 4$ states show distinct electric field dependence. a–**c**, Conductance as a function of n measured for various temperatures for $B = 0.5$ T and fixed electric fields of $E_\perp = 0$ mV nm^{-1} (**a**), $E_\perp = 15$ mV nm^{-1} (**b**) and $E_\perp = 50$ mV nm^{-1} (**c**). The density $n(\nu = -2) = -0.25 \times 10^{11}$ cm^{-2} corresponding to $\nu = -2$ at $B = 0.5$ T is indicated by the vertical line in each plot. **d**, Arrhenius plots of the conductance (normalized by its value at 10 K) measured at $n(\nu = -2)$ for $E_\perp = 0$ mV nm^{-1} (black squares), 15 mV nm^{-1} (blue squares) and 50 mV nm^{-1} (green squares) are shown. In addition, the data at $n(\nu = -4)$ and $E_\perp = 0$ mV nm^{-1} are shown with red triangles. The coloured lines are linear fits to the corresponding datasets. **e**, Electric field evolution of the activation gaps in the $\nu = 0$, $\nu = -2$ and $\nu = -4$ states. The error bars originate from the uncertainty from the linear fits.

stems from the opposite mean-field gaps in the two valleys in one of the two spin species[9–11] (Fig. 1e, Methods).

The intimate relation of the orbital magnetism to the $\nu = \pm 2$ QAH phases can be further validated by a series of test measurements. First, cyclic B sweeps for fixed n (and consequently varying ν) do not show hysteretic behaviour (Fig. 3b). These measurements were performed at $n = -0.25 \times 10^{11}$ cm^{-2}, $n = -0.5 \times 10^{11}$ cm^{-2} and $n = -1.0 \times 10^{11}$ cm^{-2} corresponding to the quantum Hall states of $\nu = -1$, $\nu = -2$ and $\nu = -4$ at $B = 1$ T, respectively. This implies that when the magnetic field is swept towards $B = 0$, the sample leaves the $\nu = -2$ QAH phase and reaches quantum Hall states with higher filling factors up to $\nu = -12$ for $n = -1.0 \times 10^{11}$ cm^{-2}, far away from the $\nu = -2$ QAH phase.

A second set of test measurements addresses the electric field dependence in the region where the $\nu = -2$ QAH phase is stable (Fig. 3c). Consistently, at $E_\perp = 0$, we do not observe any hysteretic behaviour as a $\nu = -2$ state is not observable here. At $E_\perp = -10$ mV nm^{-1}, in agreement with the observations from the fan diagrams (Fig. 2), hysteretic behaviour starts to emerge, and the hysteresis loop area reaches its maximum at $E_\perp = -17$ mV nm^{-1}. With increasing negative electric field, the hysteresis decreases again and vanishes completely at $E_\perp = -60$ mV nm^{-1}, where the fully layer-polarized $\nu = 0$ QVH phase dominates. These observations are consistent with the electric field dependence of the $\nu = -2$ state in Fig. 2 and the partial layer polarization of the $\nu = -2$ QAH phase in Fig. 1e.

Finally, the hysteretic behaviour vanishes at constant finite electric field if the filling factor is detuned substantially away from $\nu = -2$ (Fig. 3d). As the $\nu = -1$ and $\nu = -3$ quantum Hall states do not emerge at $B < 1$ T, all nominal fillings in the range of $-1 < \nu < -3$ correspond to the $\nu = -2$ state. In this range, we observe hysteresis with the loop area reaching its maximum at $\nu = -2.5$. At higher or lower nominal filling, for example, $\nu = -1$ or $\nu = -3$, the hysteresis almost vanishes.

Activation gaps depending on electric field

As a final test of the stability of the $\nu = -2$ QAH phase, we have investigated its temperature dependence at various electric fields at $B = 0.5$ T (Fig. 4); see Extended Data Fig. 8 for the full temperature-dependent

transport data. Although a quantitative estimation of the bulk gap in the $\nu = -2$ state via calculation of its activation energy $\Delta_{\nu=-2}$ is challenging due to the potential presence of disorder, we use such estimates for a relative judgement of the stability of the various observed phases. Figure 4d shows an Arrhenius plot[8] of the conductance at $n(\nu = -2)$ and various electric fields. As the temperature dependence of the conductance[23] follows $\sigma \propto \exp(-\Delta_\nu/(2k_BT))$, where T is the temperature and k_B is Boltzmann constant, in the semi-log graph we can use a linear fit to calculate the energy gap. At zero electric field (Fig. 4a), the $\nu = -2$ state does not persist to $B = 0.5$ T as we have seen in the fan diagrams, and consequently the temperature dependence is very small, indicating a vanishing energy gap. By contrast, at a finite electric field of $E_\perp = 15$ mV nm^{-1}, there is an evident temperature dependence (Fig. 4b) with an energy gap of $\Delta_{\nu=-2} = (0.09 \pm 0.02)$ meV. Applying an even higher electric field of $E_\perp = 50$ mV nm^{-1} (Fig. 4c), the $\nu = -2$ state becomes less stable with a smaller $\Delta_{\nu=-2} = (0.039 \pm 0.001)$ meV, again consistent with its predicted partial layer polarization. We point out that the gap energies measured by activation only give lower bounds for the real gaps due to the presence of local disorder (Methods), but their absolute magnitudes can be put into perspective by comparing them with the gaps of the $\nu = \pm 4$ and $\nu = 0$ states as functions of electric field, as shown in Fig. 4e. The behaviour of the $\nu = 0$ state with a large gap of $\Delta_{\nu=0} = 3$ meV at zero electric field, a vanishing gap for an intermediate electric field and a reappearance for a high electric field is consistent with the observation of the phase transition from the interaction-driven layer-balanced gapped LAF phase to the electric-field-induced fully layer-polarized gapped QVH state[23,24]. The activation gaps of the $\nu = -4$ and $\nu = -2$ states show very different electric field dependencies but rather similar magnitudes, with $\Delta_{\nu=-4} = (0.08 \pm 0.04)$ meV at $E_\perp = 0$ mV nm^{-1} and $\Delta_{\nu=-2} = (0.09 \pm 0.02)$ meV at $E_\perp = 15$ mV nm^{-1}. This observation is surprising, as in previous experiments $\Delta_{\nu=-4} > \Delta_{\nu=-2}$ has been found[30,32,38]. Whereas these previous measurements of the $\nu = \pm 2$ and $\nu = \pm 4$ states were performed at larger magnetic fields or without an independent control of $E_\perp$ and n, where the QAH $\nu = \pm 2$ phases may be unstable, the surprising robustness of the $\nu = \pm 2$ states evidenced by the larger activation gaps arises from the electric field coupling to the layer polarization and the magnetic field coupling to the orbital magnetization of the quasiparticles.

Outlook

Since the current measurements have been performed on two-terminal devices, future measurements using a four-terminal geometry[35,39] could distinguish between longitudinal and Hall resistances and determine possible switching mechanisms of the exotic ordering of such $\nu = \pm 2$ QAH phases by using both magnetic and electric fields. Finally, applications in low-dissipation electronics or quantum information science[40] could be exciting developments.

Online content

Any methods, additional references, Nature Research reporting summaries, source data, extended data, supplementary information, acknowledgements, peer review information; details of author contributions and competing interests; and statements of data and code availability are available at https://doi.org/10.1038/s41586-021-03849-w.

1. Chang, C.-Z. et al. Experimental observation of the quantum anomalous Hall effect in a magnetic topological insulator. *Science* **340**, 167–170 (2013).
2. Tenasini, G. et al. Giant anomalous Hall effect in quasi-two-dimensional layered antiferromagnet $Co_{1/3}NbS_2$. *Phys. Rev. Res.* **2** (2020).
3. Zhao, Y.-F. et al. Tuning the Chern number in quantum anomalous Hall insulators. *Nature* **588**, 419–423 (2020).
4. Tschirhart, C. L. et al. Imaging orbital ferromagnetism in a moiré Chern insulator. *Science* **372**, 1323–1327 (2021).
5. Sharpe, A. L. et al. Emergent ferromagnetism near three-quarters filling in twisted bilayer graphene. *Science* **365**, 605–608 (2019).
6. Serlin, M. et al. Intrinsic quantized anomalous Hall effect in a moiré heterostructure. *Science* **367**, 900–903 (2020).
7. Polshyn, H. et al. Electrical switching of magnetic order in an orbital Chern insulator. *Nature* **588**, 66–70 (2020).
8. Chen, G. et al. Tunable correlated Chern insulator and ferromagnetism in a moiré superlattice. *Nature* **579**, 56–61 (2020).
9. Zhang, F., Jung, J., Fiete, G. A., Niu, Q. & MacDonald, A. H. Spontaneous quantum Hall states in chirally stacked few-layer graphene systems. *Phys. Rev. Lett.* **106**, 156801 (2011).
10. Zhang, F. Spontaneous chiral symmetry breaking in bilayer graphene. *Synth. Met.* **210**, 9–18 (2015).
11. Nandkishore, R. & Levitov, L. Quantum anomalous Hall state in bilayer graphene. *Phys. Rev. B* **82** (2010).
12. Yu, R. et al. Quantized anomalous Hall effect in magnetic topological insulators. *Science* **329**, 61–64 (2010).
13. Zhang, F., Kane, C. L. & Mele, E. J. Surface state magnetization and chiral edge states on topological insulators. *Phys. Rev. Lett.* **110**, 46404 (2013).
14. Zhu, J., Su, J.-J. & MacDonald, A. H. Voltage-controlled magnetic reversal in orbital Chern insulators. *Phys. Rev. Lett.* **125**, 227702 (2020).
15. Xiao, D., Yao, W., Niu, Q. Valley-contrasting physics in graphene: magnetic moment and topological transport. *Phys. Rev. Lett.* **99**, 236809 (2007).
16. Lee, Y. et al. Tunable valley splitting due to topological orbital magnetic moment in bilayer graphene quantum point contacts. *Phys. Rev. Lett.* **124**, 126802 (2020).
17. Ju, L. et al. Tunable excitons in bilayer graphene. *Science* **358**, 907–910 (2017).
18. Shi, Y. et al. Electronic phase separation in multilayer rhombohedral graphite. *Nature* **584**, 210–214 (2020).
19. Jiang, L. et al. Soliton-dependent plasmon reflection at bilayer graphene domain walls. *Nat. Mater.* **15**, 840–844 (2016).
20. Ju, L. et al. Topological valley transport at bilayer graphene domain walls. *Nature* **520**, 650–655 (2015).
21. Geisenhof, F. R. et al. Anisotropic strain-induced soliton movement changes stacking order and band structure of graphene multilayers. Implications for charge transport. *ACS Appl. Nano Mater.* **2**, 6067–6075 (2019).
22. Moser, J., Barreiro, A. & Bachtold, A. Current-induced cleaning of graphene. *Appl. Phys. Lett.* **91**, 163513 (2007).
23. Weitz, R. T., Allen, M. T., Feldman, B. E., Martin, J. & Yacoby, A. Broken-symmetry states in doubly gated suspended bilayer graphene. *Science* **330**, 812–816 (2010).
24. Velasco, J. et al. Transport spectroscopy of symmetry-broken insulating states in bilayer graphene. *Nat. Nanotechnol.* **7**, 156–160 (2012).
25. Freitag, F., Trbovic, J., Weiss, M. & Schönenberger, C. Spontaneously gapped ground state in suspended bilayer graphene. *Phys. Rev. Lett.* **108**, 76602 (2012).
26. Nam, Y., Ki, D.-K., Soler-Delgado, D. & Morpurgo, A. F. A family of finite-temperature electronic phase transitions in graphene multilayers. *Science* **362**, 324–328 (2018).
27. Nam, Y., Ki, D.-K., Soler-Delgado, D. & Morpurgo, A. F. Electron–hole collision limited transport in charge-neutral bilayer graphene. *Nat. Phys.* **13**, 1207–1214 (2017).
28. Zhao, Y., Cadden-Zimansky, P., Jiang, Z. & Kim, P. Symmetry breaking in the zero-energy Landau level in bilayer graphene. *Phys. Rev. Lett.* **104**, 66801 (2010).
29. Li, J., Tupikov, Y., Watanabe, K., Taniguchi, T. & Zhu, J. Effective Landau level diagram of bilayer graphene. *Phys. Rev. Lett.* **120**, 47701 (2018).
30. Martin, J., Feldman, B. E., Weitz, R. T., Allen, M. T. & Yacoby, A. Local compressibility measurements of correlated states in suspended bilayer graphene. *Phys. Rev. Lett.* **105**, 256806 (2010).
31. Lee, K. et al. Bilayer graphene. Chemical potential and quantum Hall ferromagnetism in bilayer graphene. *Science* **345**, 58–61 (2014).
32. Velasco, J. et al. Competing ordered states with filling factor two in bilayer graphene. *Nat. Commun.* **5**, 4550 (2014).
33. Shi, Y. et al. Energy gaps and layer polarization of integer and fractional quantum Hall states in bilayer graphene. *Phys. Rev. Lett.* **116**, 56601 (2016).
34. Zhang, J., Nandkishore, R. & Rossi, E. Disorder-tuned selection of order in bilayer graphene. *Phys. Rev. B* **91**, 1–6 (2015).
35. Ki, D.-K. & Morpurgo, A. F. High-quality multiterminal suspended graphene devices. *Nano Lett.* **13**, 5165–5170 (2013).
36. Lee, D. S., Skákalová, V., Weitz, R. T., Klitzing, K. von & Smet, J. H. Transconductance fluctuations as a probe for interaction-induced quantum Hall states in graphene. *Phys. Rev. Lett.* **109**, 56602 (2012).
37. Kumar, M., Laitinen, A. & Hakonen, P. Unconventional fractional quantum Hall states and Wigner crystallization in suspended Corbino graphene. *Nat. Commun.* **9**, 2776 (2018).
38. Velasco, J. et al. Transport measurement of Landau level gaps in bilayer graphene with layer polarization control. *Nano Lett.* **14**, 1324–1328 (2014).
39. Ki, D.-K., Fal'ko, V. I., Abanin, D. A. & Morpurgo, A. F. Observation of even denominator fractional quantum Hall effect in suspended bilayer graphene. *Nano Lett.* **14**, 2135–2139 (2014).
40. Lian, B., Sun, X.-Q., Vaezi, A., Qi, X.-L. & Zhang, S.-C. Topological quantum computation based on chiral Majorana fermions. *Proc. Natl Acad. Sci. USA* **115**, 10938–10942 (2018).

Methods

Device fabrication

The graphene flakes were exfoliated from a highly ordered pyrolytic graphite block onto silicon/silicon dioxide (Si/SiO_2) substrates. Using optical microscopy, suitable bilayer flakes were preselected by examining the optical contrast. The flakes were scanned with scanning near-field optical microscopy to avoid any structural domain walls within the channel[19–21] that might mask fragile quantum Hall phases. The electrodes (Cr/Au, 5 nm/100 nm), top gate (Cr/Au, 5 nm/160 nm) and spacer (SiO_2, 140 nm) were fabricated by multiple steps of standard lithography techniques and electron beam evaporation. To suspend both the top gates and the bilayer graphene flakes, hydrofluoric acid was subsequently used to etch about 150–200 nm of the SiO_2. Finally, the suspended dual-gated bilayer graphene devices were loaded into a dilution refrigerator.

Electrical transport measurements

The two-terminal conductance measurements were carried out in a dilution refrigerator with a base temperature of 7 mK. Unless stated otherwise, the measurements were performed with an a.c. bias current of 0.1–10 nA at 78 Hz using Stanford Research Systems SR865A and SR830 lock-in amplifiers at a temperature of $T < 10$ mK. Gate voltages were applied using multiple Keithley 2450 SourceMeters. Several homebuilt low-pass resistor–capacitor (RC) filters were used in series to reduce high-frequency noise.

Device annealing and characterization

Current annealing procedure. Before any measurements can be performed, a current annealing procedure is used to clean the samples. Multiple cycles of current annealing at 1.6 K are performed, during which the d.c. resistance $R_{d.c.}$ of the sample is tracked (Extended Data Fig. 1a). In general, for an increasing applied d.c. voltage $V_{d.c.}$, the resistance of the sample decreases. However, when a saturation of the drain current is reached, $R_{d.c.}$ consequently increases again. The maximum current flowing was approximately 0.35 mA μm^{-1} per layer.

Measurement details. The dual-gate structure allows independent tunability of the charge carrier density n and the perpendicular electric field $E_\perp$. We can define n and $E_\perp$ as a function of the top gate voltage V_t and the bottom gate voltage V_b as follows[23]:

$$n = \frac{C_b}{e}(\alpha V_t + V_b)$$

and

$$E_\perp = \frac{C_b}{2\varepsilon_0}(\alpha V_t - V_b),$$

where ε_0 is the vacuum permittivity and $\alpha = \frac{C_t}{C_b}$ is the ratio between the top gate capacitance C_t and the bottom gate capacitance C_b. Hence, by changing V_t and V_b simultaneously, we can directly sweep n or $E_\perp$. A Lorentzian fit to a density sweep and a precise electric field sweep were used to find the exact charge neutrality point.

For the hysteresis measurements, the filling factor reads

$$\nu = \frac{nh}{e|B|} = \frac{C_b(\alpha V_t + V_b)h}{e^2|B|},$$

where h is Planck's constant and B is the magnetic field. Hence, to sweep the magnetic field while fixing the filling factor, V_t, V_b and B need to be varied simultaneously.

Calculation of the contact resistance. As in two-terminal transport measurements there always pertains a contact resistance, we calculated and subtracted it in our data. This was done by recording a resistance versus density sweep at $B = 2$ T and $E_\perp = 20$ mV nm^{-1}. Appearing resistance plateaus were assigned to a filling factor. Plotting the resistance of the quantum Hall plateaus as a function of the inverse filling factor (Extended Data Fig. 1b) gives a linear behaviour. Using a linear fit demonstrates that the slope per filling factor (25,604 ± 712) Ω fits well to the von Klitzing constant, while giving a contact resistance of $R_C = (3{,}545 \pm 161)$ Ω. For all measurements shown in this paper (except Fig. 1b), we subtracted R_C.

Quality of the device. Extended Data Fig. 1c shows the conductance of the device as a function of charge carrier density for zero and finite electric field. The narrow width and low conductance of the device at $E_\perp = 0$ mV nm^{-1} suggest a high quality of the device. Besides calculating the residual charge disorder (Fig. 1b, inset), we additionally have calculated the electron/hole mobility $\mu_{e/h} = 120{,}000/130{,}000$ $cm^2 (Vs)^{-1}$ at $n = \pm 5 \times 10^9$ cm^{-2}, emphasizing the high quality of the device.

Theoretical fundamentals regarding the ALL QAH phases

Competing ground states in bilayer graphene at $n = E_\perp = B = 0$. In bilayer graphene at $n = E_\perp = B = 0$, when spin is ignored only two different types of competing ground states can be distinguished[9–11]: one in which the K and K′ valleys are layer-polarized in the opposite sense producing a QAH phase with broken time-reversal symmetry (Θ), orbital magnetization and quantized charge Hall conductivity ($\pm 2\,e^2/h$ without counting spin degeneracy), and one in which the two valleys have the same sense of layer polarization producing a QVH phase with broken inversion symmetry (P), net layer polarization and non-trivial valley Hall conductivity. When spin is included, there are three additional types, namely the LAF phase, the ALL phase and the quantum spin Hall phase[9,10]. The five distinct phases in the spinful case can be obtained by each spin species choosing to be one of the two QVH phases or one of the two QAH phases, as depicted in Extended Data Fig. 2. These phases are distinguished[9,10] by their charge, spin, valley and spin–valley Hall conductivities, by their layer polarizations, by their orbital magnetizations, and by their broken symmetries, as summarized in Extended Data Table 1.

Quasiparticle orbital magnetism in bilayer graphene. In ABC-stacked N-layer graphene, the presence of a spontaneous gap at the Brillouin zone corners K and K′ produces non-trivial momentum-space Berry curvature, and the Berry curvature gives rise to non-trivial orbital magnetic moments of quasiparticles. The orbital magnetic moment of the quasiparticle state in band α of spin s_z, valley τ_z and momentum $\mathbf{p}$ reads[9,10]

$$m_z^{(\alpha)}(\mathbf{p}, \tau_z, s_z) = \left[-\tau_z \frac{\lambda}{h_t^2}\left(\frac{\partial h_\parallel}{\partial p}\right)^2 m_e \right]\mu_B,$$

where $h_\parallel = (v_0 p)^N/\gamma_1^{N-1}$, $h_t = (\lambda^2 + h_\parallel^2)^{1/2}$, $\gamma_1 \approx 0.4$ eV is the nearest-neighbour interlayer coupling, m_e is the electron mass, v_0 is the Fermi velocity in monolayer graphene, $\lambda\tau_z$ is the spontaneous gap term in Extended Data Table 1, $\alpha = \pm$ denote the two low-energy bands and μ_B is the Bohr magneton. Note that in the presence of a particle–hole symmetry, the moments of the particle and hole states are the same; in other words, the orbital magnetic moment does not depend on the band index α.

For AB bilayer graphene, the orbital magnetic moment reads

$$m_z^{(\alpha)}(\mathbf{p}, \tau_z, s_z) = \left[-\tau_z \frac{4\lambda m_e v_0^4 p^2}{\lambda^2\gamma_1^2 + v_0^4 p^4} \right]\mu_B,$$

With a Wannier function $|W^{(\alpha)}(\mathbf{R})\rangle = M^{-1/2}\sum_{\mathbf{k}} |\psi^{(\alpha)}(\mathbf{k})\rangle e^{i\mathbf{k}\cdot\mathbf{R}}$ at the lattice vector $\mathbf{R}$ and an energy cutoff $v_0 p \approx \gamma_1 \gg |\lambda|$, it follows that the total orbital magnetization per unit area can be defined as

$$\langle W^{(\alpha)}(\mathbf{R})|m_z^{(\alpha)}|W^{(\alpha)}(\mathbf{R})\rangle/A_{\mathrm{unitcell}} = \int m_z^{(\alpha)}(p,\tau_z,s_z)\frac{\mathrm{d}\mathbf{k}}{(2\pi)^2}$$
$$= -\tau_z\frac{\lambda m_e}{\pi\hbar^2}\ln\left(\frac{\gamma_1}{|\lambda|}\right)\mu_B,$$

where A_{unitcell} is the area of a unit cell and $\hbar$ is the reduced Planck's constant. For a spontaneous gap of 10 meV, 1 meV and 0.1 meV, the orbital magnetization per unit cell for each spin–valley species is 8.0 mμ_B, 1.3 mμ_B and 0.18 mμ_B, respectively.

Eight possible ALL QAH phases in bilayer graphene. The ALL phase in Extended Data Table 1 and Extended Data Fig. 2 can be viewed as a phase in which one spin–valley species polarizes into one layer whereas the other three species polarize into the opposite layer, or alternatively as a phase in which one spin species is in one of the two possible QVH phases (that have opposite layer polarization, for example, Extended Data Fig. 3a, b) whereas the other spin species is in one of the two possible QAH phases (that have opposite Chern numbers, for example, Extended Data Fig. 3a, f). Based on either viewpoint, one can find eight different ALL phases in total, as depicted in Extended Data Fig. 3.

Evolution of the $\nu = \pm 2$ state in electric and magnetic field

Here we show additional data on how the $\nu = \pm 2$ state behaves in an electric and magnetic field. We have recorded multiple electric field versus density conductance maps at various magnetic fields (Extended Data Fig. 4a–h). Extended Data Fig. 4a–d shows the conductance map for lower magnetic fields $B = 0.1$ T, $B = 0.2$ T and $B = 0.5$ T as well as a map with a reversed field of $B = -0.5$ T, respectively. Of the four domains observed at $B = 0.8$ T, only three show a quantized conductance of $2\,e^2\,h^{-1}$ at lower fields. The domain at negative electric field and positive density shows a higher conductance, possibly due to residual disorder providing additional channels for charge transport. Still, this domain behaves like the other three, as we also see in the fan diagrams in Fig. 2.

Changing the direction of the magnetic field (Extended Data Fig. 4c, d) shows the other four ALL phases (see also Extended Data Fig. 3).

Furthermore, from the conductance map as a function of electric field and density at different magnetic fields (Extended Data Fig. 4a–h) and the conductance map as a function of electric and magnetic fields at a fixed filling factor $\nu = -2.25$ (Extended Data Fig. 4i), we can see the evolution of the ALL phases (for example, the $\nu = -2$ state) in electric and magnetic fields. The required minimum and maximum electric fields and the electric field range for the $\nu = -2$ state to emerge increase slightly with increasing the magnetic field. At a very low magnetic field, the $\nu = -2$ state is only stable in a very limited electric field range, as at larger electric fields a fully layer-polarized $\nu = 0$ state dominates over the partially layer polarized $\nu = -2$ state. However, as the magnetic field increases, the $\nu = -2$ state becomes more and more stabilized, that is, the electric field range increases.

Lastly, we turn to the relevant physics at high magnetic fields. The $\nu = \pm 2$ states discussed in this current work appears near zero magnetic field, whereas in previous studies higher magnetic fields were applied. In fact, there are two types of $\nu = \pm 2$ quantum Hall ferromagnetic state at large magnetic fields: one without layer polarization (layer XY-like) that appears near zero electric field and the other with layer polarization (layer Ising-like) that requires a finite electric field. This was mentioned in a theoretical study[41] and observed in dual-gated devices[31,32,42]. The ALL states adiabatically evolve into the layer-polarized $\nu = \pm 2$ quantum Hall ferromagnetic states with increasing magnetic field. Although there is no transition, the required electric field range does evolve with the magnetic field.

Additional fan diagrams showing a complete electric field series

Extended Data Fig. 5 shows additional fan diagrams, demonstrating the behaviour of quantum Hall states towards zero magnetic field for various electric fields. The strength of each Landau level is indicated by the number of coloured lines with the corresponding slope in the top of each picture.

As the $\nu = \pm 4$ state is a non-layer-polarized phase, it is less and less pronounced for increasing electric field. On the contrary, as discussed already in the main text, the $\nu = \pm 2$ state is strongest for a finite range of electric fields. However, it does not emerge at $E_\perp = 0$ but appears for increasing electric fields. For $E_\perp = -10$ mV nm^{-1}, it does finally emerge for the complete magnetic field range shown here. The highest number of fluctuations corresponding to it appears at $E_\perp = -15$ mV nm^{-1} to $E_\perp = -20$ mV nm^{-1}, whereas for higher negative fields they disappear again. Lastly, the $\nu = 0$ state is strong for low electric fields (canted antiferromagnetic phase) and for very high electric fields, where it is a fully layer-polarized phase.

Evidence of the QAH effect in a second device

Extended Data Fig. 6 shows the quantum transport data measured in a second device. Extended Data Fig. 6a, b shows the conductance map for low magnetic fields of $B = 0.2$ T and $B = 0.5$ T, respectively. Although the sample is less clean than the one shown in the main text, we still see four domains with a conductance of $\pm 2\,e^2\,h^{-1}$ (four green regions in Extended Data Fig. 6a, b) even at these low magnetic fields. Furthermore, the $\nu = \pm 2$ states have the same behaviour when applying an electric field and magnetic field. Extended Data Fig. 6c shows the conductance as a function of electric and magnetic field for a fixed filling factor $\nu = -2$. The $\nu = -2$ state emerges for only intermediate applied electric fields and the range at which it appears increases with increasing magnetic field. Lastly, also in this device we see magnetic hysteresis (Extended Data Fig. 6d) when sweeping B around zero while fixing $\nu = -2$ and $E_\perp = -19$ mV nm^{-1}. However, the hysteresis is less prominent and the conductance breaks down for low magnetic fields, presumably due to the lower quality of the device.

More details on the hysteresis

At first sight, the observation of magnetic hysteresis with two-terminal measurements might be surprising, as only absolute values are measured without resolving the two components, σ_{xx} and σ_{xy}. However, following the previous derivation of the two-terminal conductance[43]

$$\sigma_{\mathrm{two-terminal}} \propto \sqrt{{\sigma_{xx}}^2 + {\sigma_{xy}}^2}$$

or, in terms of the longitudinal ρ_{xx} and Hall resistivity ρ_{xy}

$$\sigma_{\mathrm{two-terminal}} \propto \frac{1}{\sqrt{{\rho_{xx}}^2 + {\rho_{xy}}^2}},$$

one can observe a hysteresis if $\sigma^{\mathrm{forward}}_{\mathrm{two-terminal}} \neq \sigma^{\mathrm{backward}}_{\mathrm{two-terminal}}$. This is true around the coercive field, where a transition between two different ALL phases occurs, that is, $|\rho_{xx}^{\mathrm{forward}}| \neq |\rho_{xx}^{\mathrm{backward}}|$ and/or $|\rho_{xy}^{\mathrm{forward}}| \neq |\rho_{xy}^{\mathrm{backward}}|$. Around zero magnetic field, the hysteresis vanishes in two-terminal measurements, as $\rho_{xx}^{\mathrm{forward}} = \rho_{xx}^{\mathrm{backward}} = 0$ and $\rho_{xy}^{\mathrm{forward}} = -\rho_{xy}^{\mathrm{backward}}$, even though opposite orbital magnetizations (with $\rho_{xy} = \pm h/2e^2$) are present and distinguishable in four-terminal measurements[6].

To further prove the presence of the magnetic hysteresis, we have measured it for different ranges of magnetic fields, as shown in Extended Data Fig. 7. The degree of the hysteresis increases with the field range of the cycle. When the magnetic field is only swept in a small range ($-0.25\ \mathrm{T} \leq B \leq 0.25$ T), there is almost no hysteretic behaviour. However, when the magnetic field is swept from a larger field towards zero ($-0.5\ \mathrm{T} \leq B \leq 0.5$ T), the hysteresis appears partially. The fact that a sufficiently large magnetic field is needed to observe a hysteresis has been seen in twisted bilayer graphene[5,6]. The maximum degree of hysteresis is reached at $|B| \leq 1$ T and then remains nearly the same with further increasing the magnetic field range.

Temperature-dependent transport data

Extended Data Fig. 8 shows maps of the conductance as a function of electric field and density for various temperatures. The temperature-dependent data shown in Fig. 4 are taken from these measurements, with the position of the linecuts indicated by dashed lines in the top left image. In general, we see that for $T \leq 0.3$ K, the maps are basically the same, whereas for higher temperatures, the $\nu = \pm 2$ and $= \pm 4$ as well as the $\nu = 0$ states get less and less well resolved, as fluctuations due to increasing temperatures broaden all phase transitions. We point out that gap energies measured by activation can only give lower bounds for the real gaps due to the presence of local disorder. As a consequence, in some measurements (for example, Chen et al.[8]) activation gaps are—like in our case—smaller than the temperature range they are measured in. To give an estimate of thermodynamic gaps, direct measurements of the inverse compressibility would be required (Martin et al.[30]). Our gap energies should be thus understood as lower bounds and can give an estimate to compare the strength of the different phases against one another within the same sample and to get a feeling for the dependence of the gap strength as function of applied perpendicular electric field.

Data availability

The data that support the findings of this study are available from the corresponding authors upon reasonable request.

41. Barlas, Y., Côté, R., Nomura, K. & MacDonald, A. H. Intra-Landau-level cyclotron resonance in bilayer graphene. *Phys. Rev. Lett.* **101**, 97601 (2008).
42. Zibrov, A. A. et al. Tunable interacting composite fermion phases in a half-filled bilayer-graphene Landau level. *Nature* **549**, 360–364 (2017).
43. Abanin, D. A. & Levitov, L. S. Conformal invariance and shape-dependent conductance of graphene samples. *Phys. Rev. B* **78** (2008).

Acknowledgements R.T.W. and F.R.G. acknowledge funding from the Center for Nanoscience (CeNS) and by the Deutsche Forschungsgemeinschaft (DFG, German Research Foundation) under Germany's Excellence Strategy-EXC-2111-390814868 (MCQST). F.Z. and T.X. acknowledge support from the Army Research Office under grant number W911NF-18-1-0416 and by the National Science Foundation under grant numbers DMR-1945351 through the CAREER programme and DMR-1921581 through the DMREF programme.

Author contributions F.R.G. fabricated the devices and conducted the measurements and data analysis. F.Z. and T.X. contributed the theoretical part. All authors discussed and interpreted the data. R.T.W. supervised the experiments and the analysis. The manuscript was prepared by F.R.G., F.Z. and R.T.W with input from all authors.

Competing interests The authors declare no competing interests.

Additional information

Supplementary information The online version contains supplementary material available at https://doi.org/10.1038/s41586-021-03849-w.

Correspondence and requests for materials should be addressed to Fan Zhang or R. Thomas Weitz.

Peer review information *Nature* thanks Kayoung Lee, Sergey Slizovskiy and the other, anonymous, reviewer(s) for their contribution to the peer review of this work. Peer reviewer reports are available.

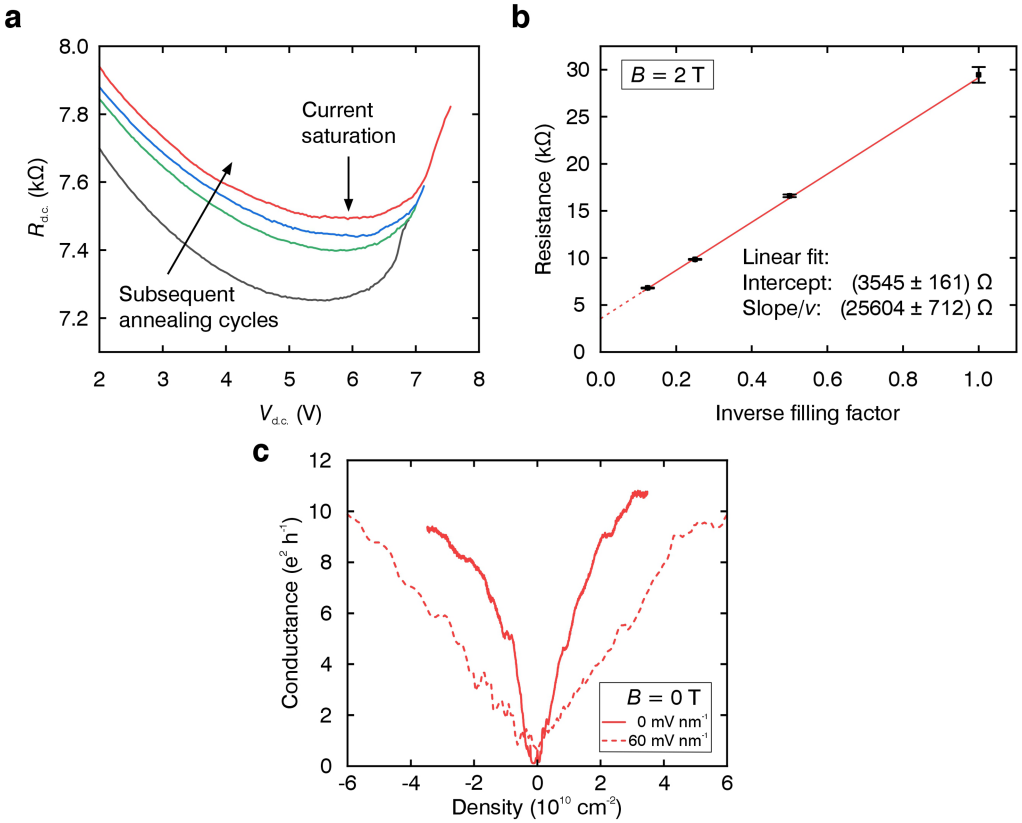

Extended Data Fig. 1 | Current annealing, contact resistance and device quality. a, $R_{d.c.}$ as a function of $V_{d.c.}$ during multiple annealing cycles. **b**, The resistance of quantum Hall plateaus shown as a function of inverse filling factor at $B = 2$ T and $E_{\perp} = 20$ mV nm^{-1}. **c**, The conductance as a function of density for $E_{\perp} = 0$ mV nm^{-1} and 60 mV nm^{-1} at $B = 0$ T.

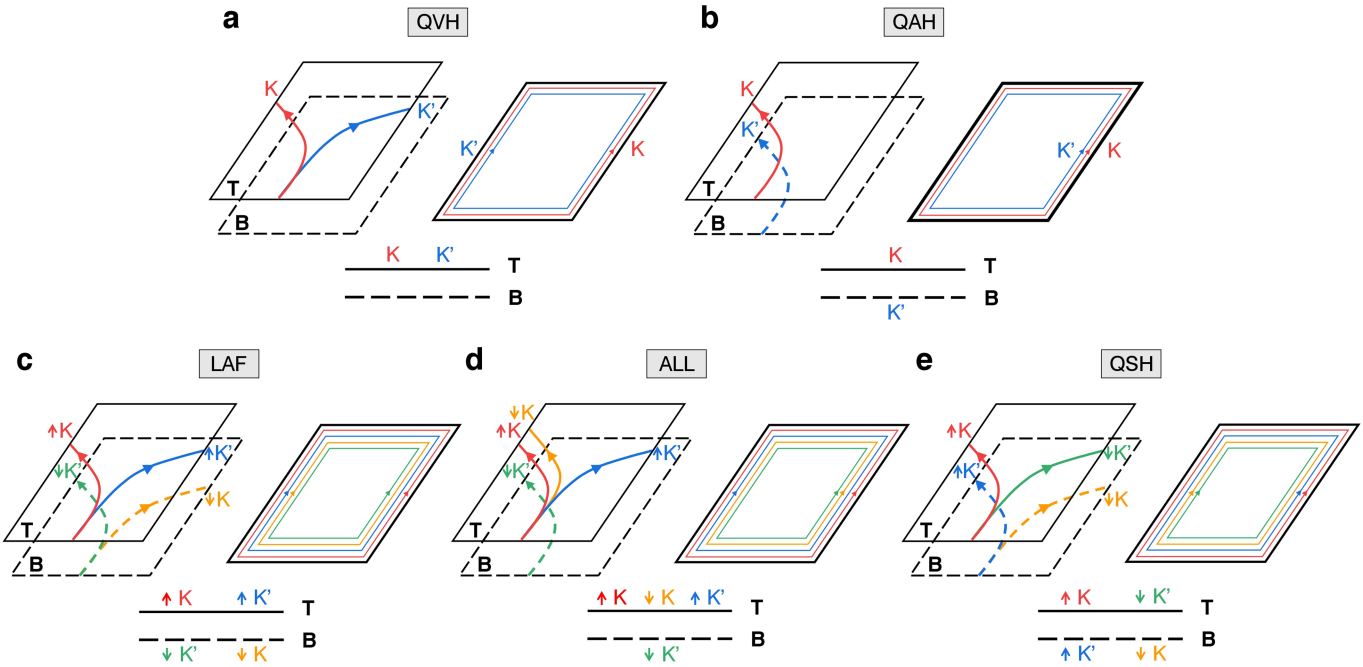

Extended Data Fig. 2 | Representatives of the five competing broken symmetry ground states in bilayer graphene at $n = E_\perp = B = 0$. a–e, Bottom panel: layer polarizations of the four spin-valley species. Top-left and top-right panels: bulk (classical) and edge (quantum) pictures of the corresponding spontaneous quantum Hall effect. Note that the edge roughness can produce couplings between counter-propagating edge states (of the same spin but different valleys) and thus gap them. Spin degeneracy is implicit in **a** and **b**. See the text for details. T and B refer to the top and bottom graphene layers, respectively.

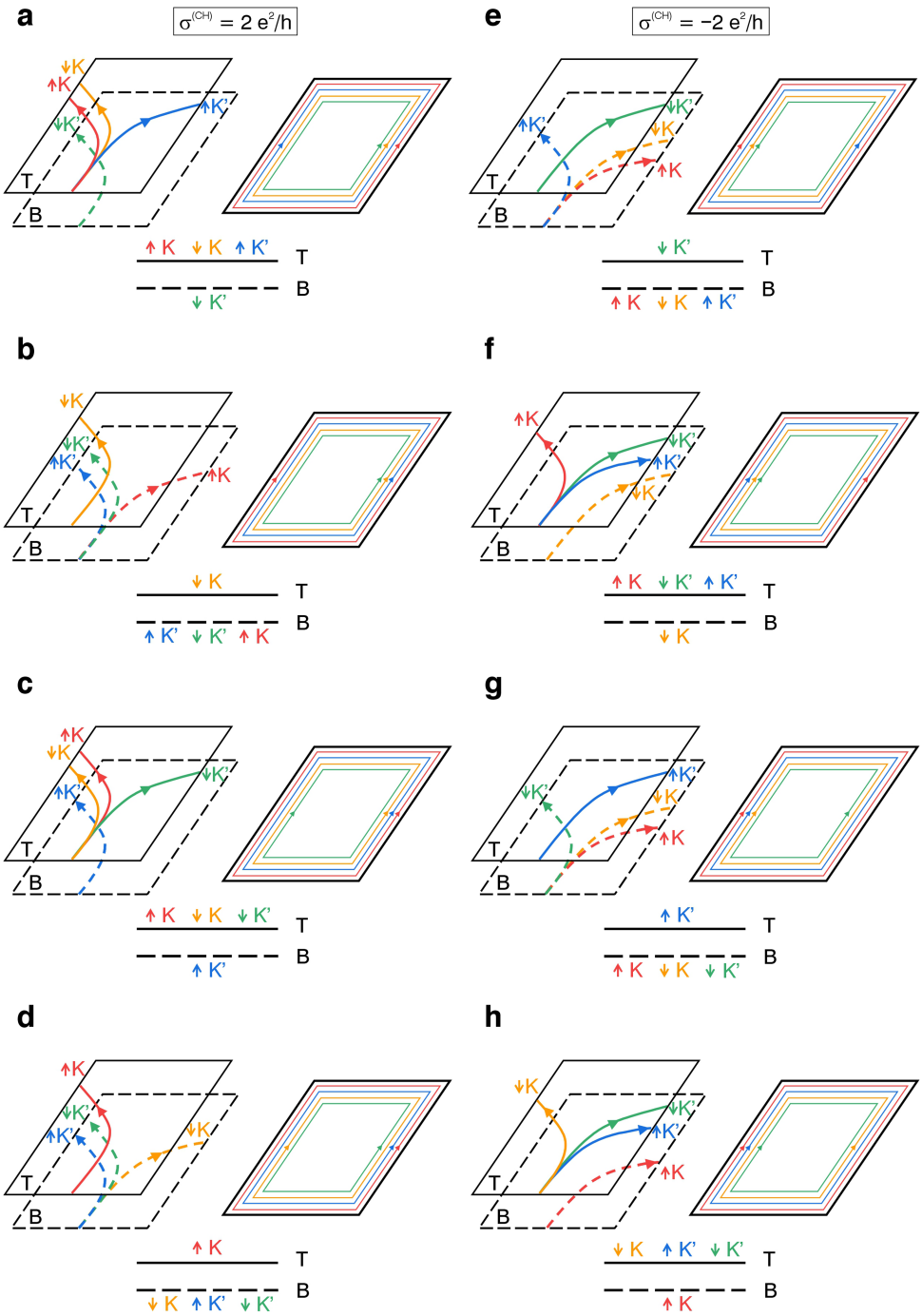

Extended Data Fig. 3 | Possible 'ALL' quantum anomalous Hall phases in bilayer graphene. a–h, Eight different 'ALL' phases that can be classified by the layer polarizations of their two spin species, by which spin species being in which QAH or QVH phases, and by their charge Hall conductivities.

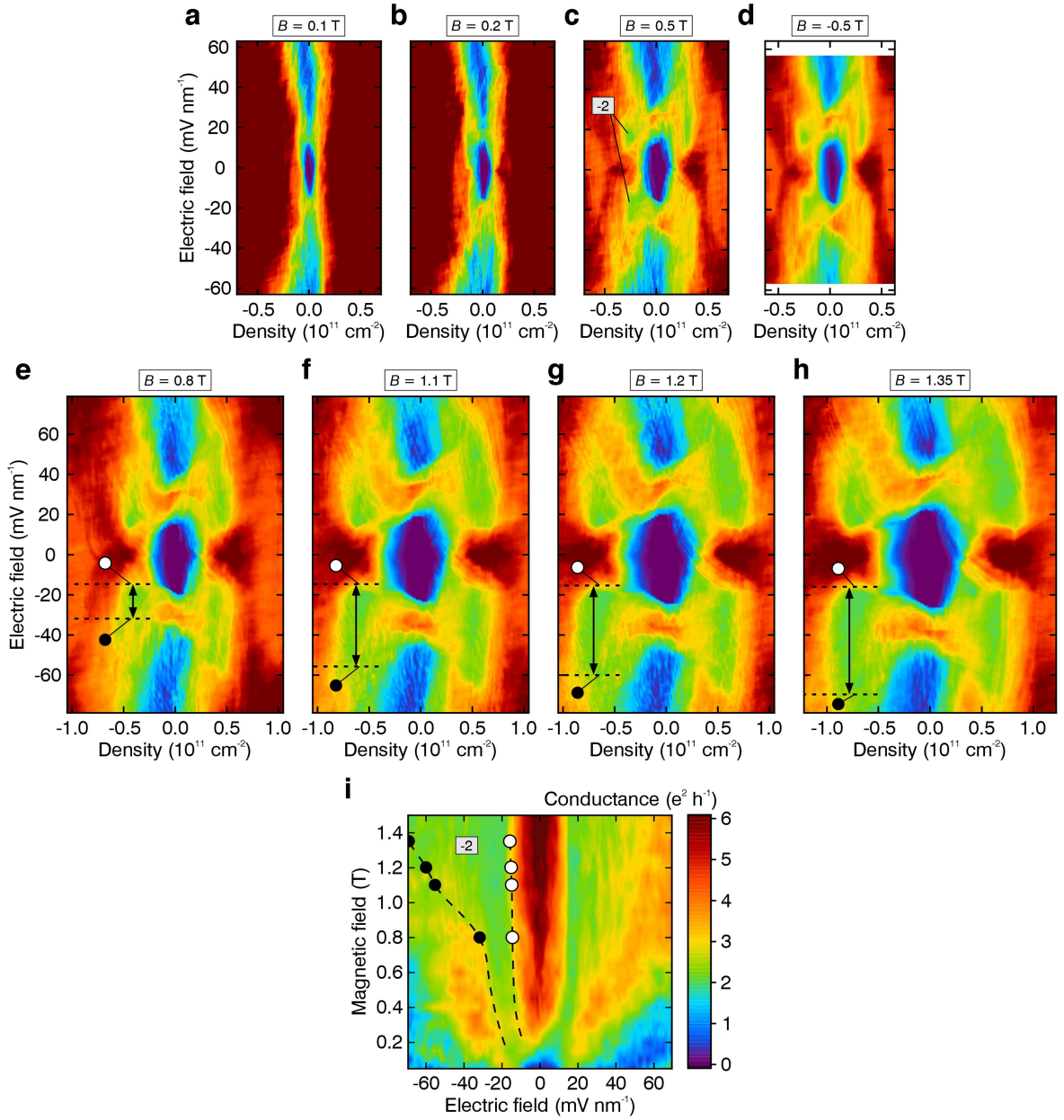

Extended Data Fig. 4 | Additional measurements showing the electric and magnetic field dependence of the $\nu = \pm 2$ state. a–**h**, Maps of the conductance as a function of electric field and density for various magnetic fields. The dashed lines in **e**–**h** are guides to the eye, and the arrows indicate the range of negative electric field at which the $\nu = -2$ state emerges. **i**, Conductance as a function of electric and magnetic fields at a fixed filling factor near $\nu = -2$ (at exactly $\nu = -2.25$). The black (white) dots indicating the maximum (minimum) electric field for the $\nu = -2$ to emerge are extracted from the data shown in **e**–**h**. The dashed lines are guides to the eye, highlighting the region where the $\nu = -2$ state emerges at negative electric fields.

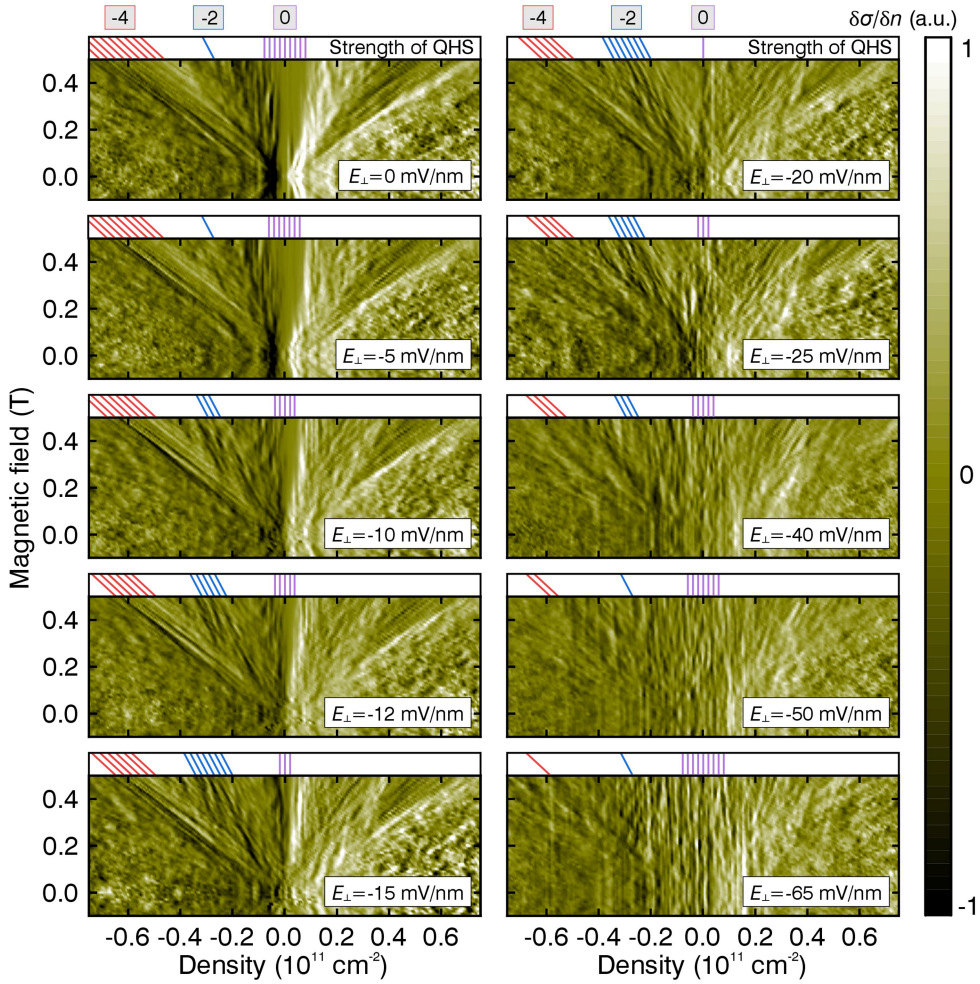

Extended Data Fig. 5 | Tracing quantum Hall states towards zero magnetic field. Derivative of the differential conductance $\delta\sigma/\delta n$ plotted as a function of magnetic field and density for various $E_\perp$. The amount of conductance fluctuations corresponding to the $\nu = 0, -2$ and -4 state are indicated by the number of white, blue and yellow lines in the top of each image.

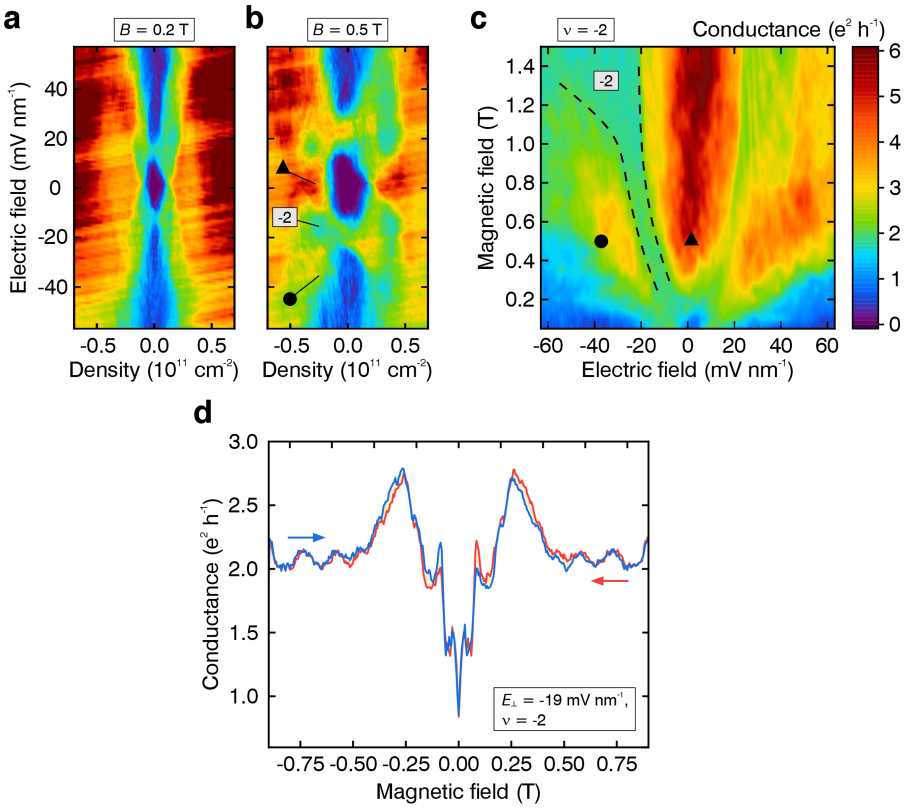

Extended Data Fig. 6 | Quantum transport data in a second device. **a**, **b**, Maps of the conductance as a function of $E_\perp$ and n for $B = 0.2$ T and 0.5 T, respectively. **c**, Conductance as a function of electric and magnetic field for fixed filling factor of $\nu = -2$. The dashed lines indicate the region where the $\nu = -2$ state at negative electric fields emerges with a conductance of $2\,e^2/h^{-1}$. **d**, Two-terminal conductance hysteresis measured for $\nu = -2$ and $E_\perp = -19$ mV nm^{-1}. The hysteresis loop area is shaded for clarity. The forward (reverse) sweep is shown in blue (red), as indicated by the arrows.

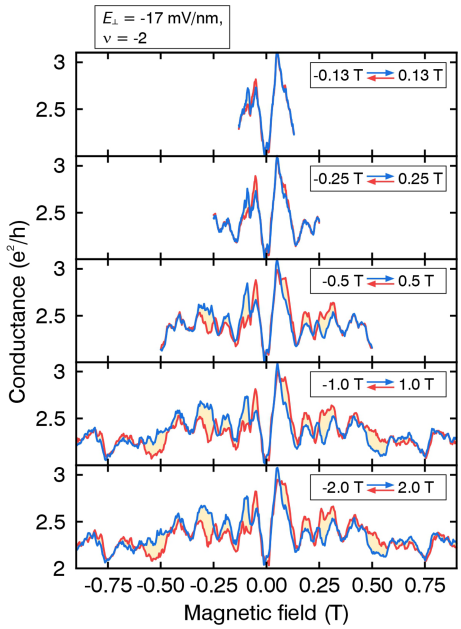

Extended Data Fig. 7 | Magnetic hysteresis loop for different magnetic field ranges. Two-terminal conductance hysteresis measured for different magnetic field ranges at $\nu = -2$ and $E_\perp = -17$ mV nm^{-1}. The hysteresis loop areas are shaded for clarity. The forward (reverse) sweep is shown in blue (red), as indicated by the arrows.

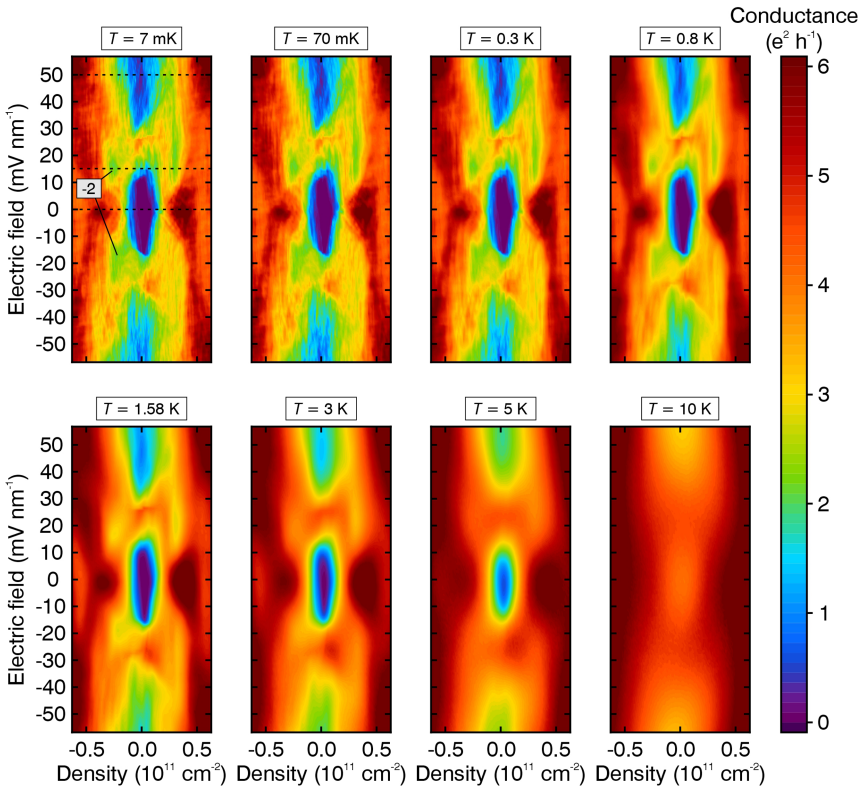

Extended Data Fig. 8 | Temperature dependence of the quantum Hall states at $B = 0.5$ T. Map of the conductance as a function of density and electric field for various temperatures. The dashed lines in the top left images indicate the position of the linecuts shown in Fig. 4 in the main manuscript.

Extended Data Table 1 | Classification of the five competing broken symmetry ground states in bilayer graphene at $n = E = B = 0$

Phase	K ↑	K ↓	K′ ↑	K′ ↓	Broken symm.	Mass ($\lambda\tau_z$)	$\sigma^{(CH)}$	$\sigma^{(SH)}$	$\sigma^{(VH)}$	$\sigma^{(SVH)}$
QVH	T	T	T	T	P	$m\sigma_z$	0	0	$2N$	0
QAH	T	T	B	B	Θ	$m\tau_z\sigma_z$	$2N$	0	0	0
LAF	T	B	T	B	$\Theta, P, SU(2)$	$ms_z\sigma_z$	0	0	0	$2N$
QSH	T	B	B	T	$SU(2)$	$m\tau_z s_z\sigma_z$	0	$2N$	0	0
"ALL"	T	T	T	B	$\Theta, P, SU(2)$	$m\left(\frac{1+\tau_z}{2}+\frac{1-\tau_z}{2}s_z\right)\sigma_z$	N	N	N	N

These phases are distinguished by their spin-valley layer polarizations, by the symmetries they break, by their order parameters, and by their charge Hall (CH), spin Hall (SH), valley Hall (VH), and spin-valley Hall (SVH) conductivities. The results are general for ABC-stacked N-layer graphene[9,10,18] and with N=2 for AB bilayer graphene.